Journal of
MATERIALS RESEARCH

Structure of nanocrystalline palladium and copper studied by small angle neutron scattering

P. G. Sanders[a)] and J. R. Weertman
Materials Science and Engineering Department, Northwestern University, Evanston, Illinois 60208-3108

J. G. Barker
Cold Neutron Research Facility, National Institute of Standards and Technology, Gaithersburg, Maryland 20899

(Received 26 February 1996; accepted 13 June 1996)

The structure of nanocrystalline palladium and copper, made by inert gas condensation and compaction, was studied using small angle neutron scattering (SANS), optical microscopy, and scanning electron microscopy. The effects of annealing and warm compaction were also examined with these techniques. The SANS results were interpreted using a maximum entropy routine, combined with knowledge of the Archimedes density and hydrogen concentration determined by prompt gamma activation analysis (PGAA). Similar hydrogen concentrations were detected by SANS and PGAA. This hydrogen content, which was approximately 5 at. % in samples compacted at room temperature, was reduced by both annealing and warm compaction. Defects in several size classes were observed, including missing grain pores (≈1–50 nm diameter) and defects of micrometer size. Warm compaction produced a lower number density of pores in nanocrystalline palladium, which led to increased density. The observed structure was correlated with Vickers microhardness and fracture surface morphology.

I. INTRODUCTION

Nanocrystalline (*n*-) materials have grain or crystallite sizes in the range of 5 to 50 nm. This small grain size leads to a larger interfacial area per unit volume, so that for a 5 nm grain size, ≈50% of the atoms are within 0.5 nm of one or more grain boundaries. This unique structure may be responsible for many reported changes in observed properties, such as increases in specific heat, thermal expansion coefficients, and diffusion coefficients.[1] However, it is important to remember that these differences may be due to either intrinsic effects (grain size or interfacial volume) or to extrinsic effects (usually resulting from processing). In the case of inert gas condensation, these extrinsic effects are usually related to the consolidation of powders. The compacted materials still exhibit the traditional powder processing problems such as pores between the grains and impurities on the particle surfaces. These defects persist to some extent despite the extremely small size of the powders, the very high compaction pressures, and the high vacuum processing. Most studies of nanocrystalline materials aim to understand the changes in intrinsic properties; that is, those brought about by the tremendous decrease in grain size and the resultant increase in interfacial area. However, the intrinsic changes may be masked or distorted by the presence of extrinsic defects.

There has been extensive debate over the structure of the numerous grain boundaries in *n*-materials. Initial reports, based on x-ray diffraction from *n*-Fe[2] and extended x-ray absorption fine structure (EXAFS) of *n*-Cu and *n*-Pd,[3] indicated that the interface structure in *n*-metals was fundamentally different, with a highly disordered or gas-like arrangement of atoms in the boundary. More recent studies, which probed the structure of *n*-Pd with x-ray diffraction[4] and high resolution microscopy,[5] as well as new EXAFS data from *n*-Cu,[6] indicated that the atomic displacements in the grain boundaries were very small and similar to those in coarser-grained materials.

This debate over grain-boundary structure has affected the interpretation of small angle neutron scattering (SANS) data. An initial SANS study on *n*-Pd[7] concluded that the observed scattering could originate from low-density, gas-like grain boundaries. A later report on SANS from *n*-Pd acknowledged the fact that the presence of pores could impact the results.[8] More recent SANS studies have interpreted the data in terms of a distribution of pores[9,10] and have found good agreement between the volume fraction of pores from SANS and Archimedes-type density measurements. Considering the

[a)]Current address: Technology Development Division, Argonne National Laboratory, Argonne, Illinois 60439-4841.

 © 1996 Materials Research Society

https://doi.org/10.1557/JMR.1996.0395 Published online by Cambridge University Press

synthesis method of inert gas condensation and compaction, it is reasonable to expect that porosity will be present. In addition, positron annihilation spectroscopy (PAS) of *n*-Pd and *n*-Cu[11,12] has identified three different size classes of voids, the largest most likely corresponding to pores with a size in the detectability range of SANS. Recent SANS studies of nanocrystalline ceramics have also attributed most of the observed scattering contrast to porosity.[13]

The long range goal of this research is to quantify the intrinsic mechanical properties of *n*-Cu and *n*-Pd. Before this can be done, the processing flaws must be reduced so that they do not obscure the intrinsic behavior. The existing defects must be quantified, and then processing improvements implemented to reduce the flaw population. The present paper reports on the first stage of a two-phase study, in which both the synthesis chamber and the compaction unit in the inert gas condensation equipment were redesigned to reduce the impurity level and increase the sample density. Improvements in samples made using the new compaction unit will be presented in this paper. The primary processing benefits of the compaction unit are that it is actively pumped and has a die that can be heated.[14] (The old unit had a static vacuum and the die was not heated.[15]) Additional studies to examine the impact of cleaner synthesis conditions are in progress.

II. EXPERIMENTAL METHODS

Nanocrystalline powders were synthesized by inert gas condensation[16] followed by *in situ* compaction[17] at Argonne National Laboratory.[14,15] After pumping the chamber to about 4×10^{-5} Pa (3×10^{-7} Torr), the chamber was back-filled with ≈660 Pa (5 Torr) of high-purity (99.999%) helium. High-purity palladium wire (99.997%) and copper shot (99.999%) were evaporated from resistively heated, alumina-lined Mo boats, with the resulting metal clusters collected on a liquid nitrogen-cooled cold finger. The clusters were removed from the cold finger with a teflon scraper and then compacted under uniaxial pressure to produce disk-shaped samples 9 mm in diameter and typically 0.1 to 0.2 mm thick. All the room temperature-compacted *n*-Pd samples were consolidated in the "old" system. In this case the compaction was performed in a two-step process, with the second, high-pressure stage carried out at 1.4 GPa in a static vacuum.[15] The outer 0.25 mm circumference of these samples was typically not as dense as the inner part of the disk. The remaining specimens were compacted in a single-stage process with active pumping, in which the base pressure was $\approx 4 \times 10^{-4}$ Pa (3×10^{-6} Torr).[14] The compaction temperatures ranged from room temperature (RT) to 300 °C, with warm compaction being denoted by (WC). The resultant samples usually had an extruded (raised) rim around the circumference on the side of the moving piston and were uniformly dense throughout. In contrast to the two-stage compaction, in which the pressure release rate was very rapid, the single-stage compaction allowed for the controlled reduction of the consolidation pressure. The primary differences between the specimens listed in Table I are the processing conditions and the grain size.

Two room temperature-compacted *n*-Pd samples were electrodischarge machined into quarters; one quarter received no further treatment, while the other three were annealed (signified by A) at 100, 300, or 800 °C for 100 min in flowing, high purity (99.999%) Ar. One room temperature-compacted *n*-Cu specimen was annealed at 150 °C for ≈9 h in a rough vacuum inside the SANS apparatus.

The grain size was determined from broadening of the 111 and 222 x-ray peaks using the Warren–Averbach method.[18,19] The broadening contributions from instrumental and root-mean-squared strain were corrected for, but those from twins and stacking faults were not. Archimedes' density, reported as the percent decrement from a fully dense, coarse-grained standard, was determined by weighing in air and ethyl phthalate, with special care taken to minimize thermal drift in the liquid measurements.[20] The results from measurements on the thicker, more massive samples were more accurate, since the change in mass between the air and liquid measurements was larger than for the thinner samples and quarter pieces.

The as-compacted samples and fracture surfaces were observed with a Hitachi S-4500 field-emission scanning electron microscope (FE-SEM) operated at 20 kV. Defects in the micrometer size range were quantified using optical microscopy and image analysis, with the area, average diameter, and aspect ratio of the pores determined at 200×. The hydrogen impurity level in the samples was measured using prompt gamma activation analysis (PGAA) at the Cold Neutron Research Facility at the National Institute of Standards and Technology[21] (NIST), while the oxygen concentration was determined with fast neutron activation analysis (FNAA) in the Department of Chemistry at the University of Kentucky.[22] (Neither PGAA nor FNAA gives information on the chemical state of the contaminants.)

SANS measurements were carried out on the 30 m NSF SANS instrument at NIST.[23] Data were collected over q ranges extending from about 0.01 to 5.7 nm^{-1}. (The magnitude of the scattering vector q is $(4\pi/\lambda) \sin \theta$, where λ is the neutron wavelength and 2θ is the scattering angle.) The wavelength ranged from 0.5 to 1.4 nm ($\Delta\lambda/\lambda = 30\%$), sample-to-detector distances were between 1.3 and 13.2 m, and the specimens were generally 0.1 to 0.2 mm thick (no samples were stacked).

https://doi.org/10.1557/JMR.1996.0395 Published online by Cambridge University Press

TABLE I. Sample processing parameters.

Sample	Material	Compaction Method	Compaction Temperature	Grain size (nm)	Annealing treatment
1PdRT	Pd	2-stage	RT	4.4	Cut into quarters, three of which were annealed
2PdRT	Pd	2-stage	RT	5.7	Cut into quarters, three of which were annealed
3PdRT	Pd	2-stage	RT	17.6	
4PdRT	Pd	2-stage	RT	18.9	
Pd100WC	Pd	1-stage	100 °C	6.3	
Pd300WC	Pd	1-stage	300 °C	10.1	
1CuRT	Cu	1-stage	RT	12.3	
2CuRT	Cu	1-stage	RT	7.8	150 °C for 9 h
Cu100WC	Cu	1-stage	100 °C	9.1	
Cu150WC	Cu	1-stage	150 °C	11.1	

A series of 10 Vickers microhardness measurements spaced 0.25 mm apart were made on each sample with a load of 100 g and a dwell time of 20 s. All reported errors are 1 standard deviation, with those for density, image analysis, and hardness being the standard deviation from the average of the individual measurements. The errors in SANS, PGAA, FNAA, and x-ray were propagated from counting statistics.

III. SANS DATA ANALYSIS

The raw SANS data were corrected for background and empty cell scattering and then converted to values of differential scattering cross section using the SANS data reduction software at NIST.[23] A plot of the logarithm of the absolute differential scattering cross section ($d\Sigma/d\Omega$) vs scattering vector for two room temperature-compacted n-Cu samples is shown in Fig. 1, after background subtraction. Two qualitative differences between the curves are evident. The first is the overall lower scattering intensity of 1CuRT; the second is the considerable leveling of the 1CuRT curve between q values of 0.07 to 0.2/nm. Tentatively, these features can be correlated with the higher overall sample density and reduced concentration of larger scattering entities in 1CuRT.

In a ln $d\Sigma/d\Omega$ vs ln q plot for room temperature and warm compacted n-Pd (Fig. 2), the progressive effects of higher compacting temperatures can be seen. Comparison of the room temperature and 100 °C compaction data shows that the scattering is about the same at high q, but reduced in the latter sample at low q. After compaction at 300 °C, scattering over the whole q-range is dramatically reduced. As the compaction temperature increases, the observed changes in differential scattering intensity can be related to a lower volume fraction of scattering objects.

The scattering data were first analyzed using the Porod relation and the invariant. The Porod relation[24] is

$$\frac{d\Sigma}{d\Omega}(q) = \frac{2\pi(\Delta\rho)^2}{q^4} \cdot \frac{S}{V} + \frac{n\sigma_{\text{inc}}}{4\pi}, \qquad (1)$$

where $(\Delta\rho)$ is the difference in the scattering length density between the matrix and the scattering entity, S/V

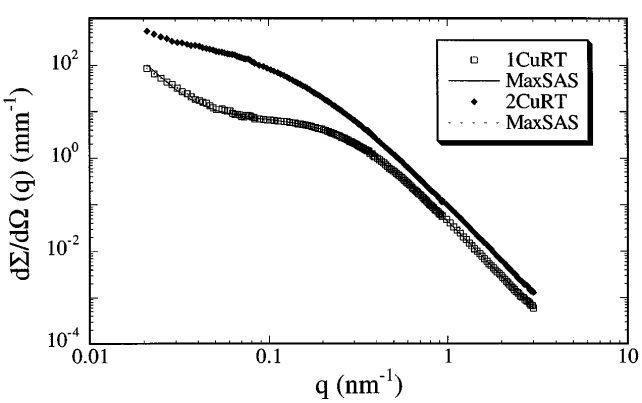

FIG. 1. Log of the differential scattering cross section $d\Sigma/d\Omega$ vs log of the scattering vector q for room temperature-compacted n-Cu with error bars and fits from the MaxSAS routine.

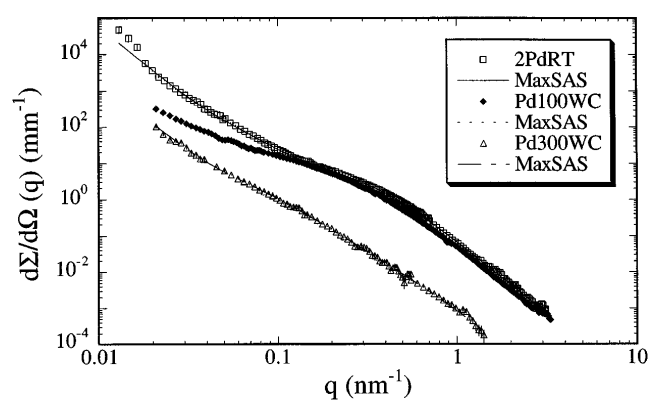

FIG. 2. Log of the differential scattering cross section $d\Sigma/d\Omega$ vs log of the scattering vector q for room temperature and warm compacted n-Pd with error bars and fits from the MaxSAS routine.

https://doi.org/10.1557/JMR.1996.0395 Published online by Cambridge University Press

is the total surface area of scatterers per unit sample volume, n is the number of atoms per unit volume, and σ_{inc} is the incoherent scattering cross section. This relation is valid for $qR \geqslant$ about 3, where R is the radius of the scattering object. For this analysis, a plot of $(d\Sigma/d\Omega)q^4$ vs q^4 was made, with the slope yielding the incoherent scattering, and the intercept giving the Porod constant C_p $[C_p = 2\pi(\Delta\rho)^2 S/V]$.

It can be seen from Fig. 2 that the scattering from 2PdRT and Pd100WC exhibits Porod behavior (slope of 4) for $q > 0.4$ nm^{-1}. Sample Pd300WC appears to be just reaching the Porod region at the highest measured q values. At lower q's all the curves bend over toward a Guinier region before an upturn at the lowest q values that is associated with a few large (>1 μm) flaws. The constant background observed at high q's ($q >$ 3.5 nm^{-1}) is thought to result from incoherent scattering.

The invariant (Q) was used to calculate the volume fraction (V_V) of scatterers,[24] with

$$Q = \int_0^\infty q \frac{2d\Sigma}{d\Omega}(q)\,dq$$

$$V_V(1 - V_V) = \frac{Q}{2\pi(\Delta\rho)^2}\,. \qquad (2)$$

The data were extrapolated to $q = 0$ with the Guinier relation[25] fit to the first few data points and to $q = \infty$ using C_p determined from Eq. (1). The major contribution to Q was from the collected data and not from extrapolations. Assuming spherical scatterers and using S/V and V_V from above, an average radius $[\overline{R} = 3\,V_V/(S/V)]$ of the scatterers could be estimated. Note that $\overline{R} = \langle R^3\rangle/\langle R^2\rangle$, and is thus weighted toward larger scatterers.

To analyze the SANS data, the microstructural features responsible for the scattering must be determined. (SANS can detect microstructural features in the size range of about one to several hundred nanometers,[23] provided that their scattering length densities differ from that of the matrix.) Based on the assumption that the SANS arose mostly from pores (as discussed in the Introduction), $\Delta\rho$ was taken to be ρ_{Pd} or ρ_{Cu}, since $\rho_{\text{pore}} = 0$. After doing the calculations described above, it was found that there was good agreement between the pore volume fraction from the invariant and that from Archimedes' density, which implied that pores were most likely the scatterers in these samples. The size range of the pores calculated from the scattering experiments was well within the detectability range of SANS.

After completing the above calculations, size distributions were determined using the maximum entropy routine developed by Potton *et al.*[26] Evaluation of the linear inverse problem utilizing the SANS data and the form factor yields the size distribution. This solution is obtained by maximizing the difference between the configurational entropy and the chi-squared minimization parameter. The actual code employed, which was written by P. R. Jemian and entitled MaxSAS,[27] solves for the volume-averaged size distribution; the number-averaged distribution is calculated from geometry. The data were fitted with a globular form factor,[28] which describes the scattering from randomly oriented globular scatterers while minimizing the Bessel function oscillations inherent in the spherical form factors.[29] The globular form factor reduces to the exponential form of the Guinier relation as $qr \rightarrow 0$ and the q^{-4} behavior of the Porod approximation as $qr \rightarrow \infty$.[29] The size range of the generated distributions was chosen such that the Guinier region was reached at low q and the Porod region was achieved at high q.

Although some features that look like pores have been observed with the transmission electron microscope,[30] it is very hard to get an accurate view of the pore shape in three dimensions, especially considering the possible impact of thin-foil preparation on the resultant pore morphology. Since the actual shape of the pores was not known, an aspect ratio of one was chosen for the calculations. Once again, there was good agreement between the volume fraction of scatterers obtained from SANS (this time using the MaxSAS routine) and the porosity determined from Archimedes' density (Table II). The good agreement of the background level and volume fraction of scatterers between the Porod/invariant and maximum entropy methods indicates that the form factor choice is appropriate. The MaxSAS fits to the data are shown as solid lines in Figs. 1 and 2. All SANS fit parameters reported in this paper were obtained from the MaxSAS routine.

On the second trip to NIST, scattering intensities were collected out to higher q's ($\approx$5.7 nm^{-1}). A large, constant background was seen with most of the samples. The suspicion that hydrogen impurities may cause this high background (hydrogen has a very large incoherent cross section) was verified by PGAA measurements. Good agreement was found between the PGAA results and the hydrogen levels calculated from the SANS background (Table III). The earlier interpretation[10] that the high-q scattering arises from very small pores $\approx$1 nm in diameter was incorrect. Such small pores probably are present in the samples,[11,12] but they are at the limit of the SANS resolution, and their presence is obscured by the hydrogen scattering. The conclusions[10] for the larger, grain-size pores still hold.

IV. RESULTS AND DISCUSSION

The hydrogen impurity level, density, and pore distribution were determined as a function of processing conditions. Changes in the microstructure as a result of annealing and warm compaction will be examined.

https://doi.org/10.1557/JMR.1996.0395 Published online by Cambridge University Press

TABLE II. SANS from room temperature and warm compacted *n*-Pd and *n*-Cu.

Sample	Archimedes' density V_V (%)	Grain diameter (nm)	SANS measurements		
			MaxSAS V_V (%)	Pore diameter[a] (nm)	H (at. %)
1PdRT	8 ± 2	4.4 ± 0.1	4.0 ± 0.9	4.9 ± 1.5	4.4 ± 0.2
2PdRT	13 ± 2	5.7 ± 0.1	11.0 ± 0.5	8.0 ± 1.8	7.8 ± 0.2
3PdRT		17.6 ± 0.2	10.0 ± 0.3	10.7 ± 3.5	4.3 ± 0.2
4PdRT		18.9 ± 0.3	12.2 ± 0.2	8.9 ± 1.9	6.7 ± 0.2
Pd100WC	8.6 ± 0.2	6.3 ± 0.1	8.1 ± 0.1	6.2 ± 2.7	5.8 ± 0.2
Pd300WC		10.1 ± 0.2	0.2 ± 0.1	4.5 ± 2.7	1.0 ± 0.2
1CuRT	2.5 ± 0.2	12.3 ± 0.2	2.7 ± 0.1	7.8 ± 2.3	2.8 ± 0.2
2CuRT	9.7 ± 0.1	7.8 ± 0.1	8.4 ± 0.1	5.8 ± 4.3	6.9 ± 0.2
Cu100WC		9.1 ± 0.1	5.0 ± 0.1	3.7 ± 2.9	4.9 ± 0.2
Cu150WC	8.1 ± 0.1	11.1 ± 0.1	6.4 ± 0.1	4.1 ± 3.5	5.7 ± 0.2

[a]Number-weighted mean diameter and standard deviation (of bin average).

A. Room temperature compaction

As previously mentioned, the hydrogen levels as measured by SANS and by PGAA were in reasonably good agreement (Table III), so the incoherent SANS background can be attributed to hydrogen. Hydrogen levels from SANS for room temperature-compacted *n*-Pd and *n*-Cu are shown in Table II; the concentration averages about 5 at. %. These measurements are in general agreement with the gaseous impurity levels reported by Gleiter[1] and the hydrogen level reported by Tschöpe and Birringer.[31]

There was good agreement between the density decrement, as measured by Archimedes' principle, and the volume fraction of scatterers from SANS (Table II). However, the MaxSAS porosity was generally lower than that from Archimedes' method, probably because the scattering from larger (≈1 μm) pores (as seen in Fig. 2 at low q) is not observed with SANS.

The grain sizes of the two-stage, room temperature-compacted *n*-Pd ranged from about 4 to 19 nm, while the average pore size was about 5 to 11 nm (Table II). A comparison of pore size and grain size shows that the pore size roughly scales with the grain size [Fig. 3(a)]. The number density of pores decreased as the grain size increased, similar to the trend of decreasing number density of grains with increasing grain size. These observations support the labeling of these pores as missing grains.[11,12] This trend of pore distribution scaling with grain size has also been noted in nanocrystalline ceramics.[13] The single-stage, room temperature-compacted *n*-Cu showed a similar trend of increasing pore size with grain size [Fig. 3(b)]. The

TABLE III. Impurities in *n*-Pd and *n*-Cu.

Sample	H (at. %) SANS	H (at. %) PGAA	O (at. %) FNAA
Pd100WC	5.8 ± 0.2	4.5 ± 1.3	0.8 ± 0.3
Pd300WC	1.0 ± 0.2	<2.1	
Pd200WC[a]		0.1 ± 0.5	1.2 ± 0.2
Cu100WC	4.9 ± 0.2	6.3 ± 0.6	
Cu150WC	5.7 ± 0.2	4.8 ± 0.9	4.1 ± 0.5
Cu150WC[a]		0.2 ± 0.8	

[a]Warmed powder prior to compaction.

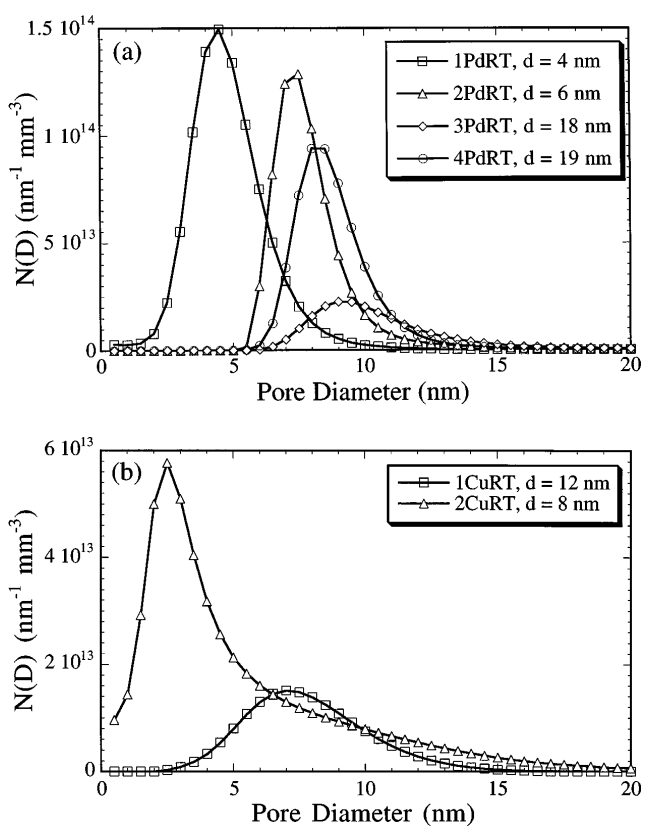

FIG. 3. Number-weighted pore distributions from the MaxSAS routine for room temperature-compacted *n*-Pd (a) and *n*-Cu(b).

https://doi.org/10.1557/JMR.1996.0395 Published online by Cambridge University Press

increased density of 1CuRT may result from its greater thickness which allows for more particle rearrangement during compaction, and its lower hydrogen level which promotes sintering of the particles through lower concentrations of surface impurities and by minimization of bubble formation (pores filled with gas).[32]

B. Annealing studies

The SANS measurement revealed that the hydrogen content decreased with increasing annealing temperature in the *n*-Pd (Table IV). This reduction in hydrogen content with annealing is analogous to the baking treatment given to steel to remove hydrogen.[33] The decrease in hydrogen with annealing implies that most of the hydrogen had not reacted with the metal and was able to diffuse out at elevated temperatures.

The density of 2PdRT annealed at 100, 300, and 800 °C was measured using Archimedes' principle and showed no significant changes, considering the ±2% error (Table IV). This is not surprising because most of the sintering at these temperatures occurs by surface diffusion, which does not lead to pore shrinkage.[32] However, Archimedes' observations are in contrast to the SANS results, which showed that the volume fraction of pores decreased substantially with increasing annealing temperature (Table IV). The most likely explanation is that as the annealing temperature increased, the pores coalesced and gradually grew beyond the detectability range of SANS (which was about 50 nm in this experiment). Fracture surfaces of samples broken by bending (Fig. 4) support this trend of increasing pore size with annealing. Larger pores developed in samples annealed at 300 and 800 °C [Figs. 4(c) and 4(d)], with the 800 °C anneal [Fig. 4(d)] clearly producing pores in the micrometer size range. Tschöpe and Birringer[31] have observed large "bubbles" (closed pores) after annealing *n*-Pt at 800 °C, while Qin *et al.*[34] attributed an increase in porosity after annealing at 500 °C to the formation of bubbles in *n*-Ag. The appearance of these large bubbles after high temperature anneals may be driven by the presence of the gases adsorbed on the clusters during synthesis. The smaller pores thought to be present in the as-produced and 100 °C anneal are very difficult to see in SEM, considering the scale of the microstructure and the intergranular nature of the fracture. (Figure 4 will be discussed further in the final section).

To quantify the size and volume fraction of the larger pores, image analysis was done on optical micrographs of the four quarters of 2PdRT after polishing about 0.08 mm off of the flat surface (about 1/2 the thickness). The pore aspect ratio for all the quarters was 2.3 ± 1.2 in the plane of the analysis (the aspect ratio along the surface normal was not examined). The area fraction of pores in the 1 to 50 μm size range was about 2% for room temperature-compacted, 100, and 300 °C annealed samples, which is about the difference between V_V from the MaxSAS and Archimedes' methods. However, the quarter annealed at 800 °C had an area fraction of pores of 4.5%, significantly higher than the others. A plot of the pore diameter distribution showed that the 800 °C anneal produced about 10 times the number of 2–4 μm pores compared to the other quarters (Fig. 5). The large increase in 2–4 μm pores may be due to the coarsening of smaller pores during the initial stage of sintering. Difficulties in quantifying the nonuniform porosity present after annealing at 800 °C [Fig. 4(d)] may account for the lower volume of pores calculated from image analysis and SANS compared to the total porosity measured using the Archimedes method (Table IV).

SANS results from the 2 *n*-Pd samples that were cut into quarters and annealed (1Pd and 2Pd) are shown in Figs. 6(a) and 7. The two sets of samples showed similar behavior, with pore size and grain size increasing with annealing temperature. The number density of pores decreased with increasing grain size (i.e., decreasing number density of grains), and the size distributions generally

TABLE IV. SANS from room temperature-compacted and annealed *n*-Pd and *n*-Cu.

			SANS measurements		
Sample	Archimedes' density V_V (%)	Grain diameter (nm)	MaxSAS V_V (%)	Pore diameter[a] (nm)	H (at.%)
1PdRT	8 ± 2	4.4 ± 0.1	4.0 ± 0.9	4.9 ± 1.5	4.4 ± 0.2
1Pd100A		4.1 ± 0.2	5.2 ± 0.7	6.5 ± 1.5	
1Pd300A		10.1 ± 0.3	4.8 ± 0.8	8.7 ± 3.9	
1Pd800A		70 ± 2	0.6 ± 1.7	10.6 ± 3.6	1.7 ± 0.3
2PdRT	13 ± 2	5.7 ± 0.1	11.0 ± 0.5	8.0 ± 1.8	7.8 ± 0.2
2Pd100A	14 ± 2	7.2 ± 0.2	9.0 ± 0.5	7.9 ± 1.7	4.7 ± 0.2
2Pd300A	10 ± 2	18.3 ± 0.2	7.4 ± 0.6	12.4 ± 4.0	2.0 ± 0.2
2Pd800A	11 ± 2	87 ± 2	0.4 ± 1.3	16.9 ± 1.5	0.5 ± 0.2
2CuRT	9.7 ± 0.1	7.8 ± 0.1	8.4 ± 0.1	5.8 ± 4.3	6.9 ± 0.2
2Cu150A	9.7 ± 0.2	10.5 ± 0.1	8.5 ± 0.1	13.4 ± 5.2	6.6 ± 0.2

[a]Number-weighted mean diameter and standard deviation (of bin average).

https://doi.org/10.1557/JMR.1996.0395 Published online by Cambridge University Press

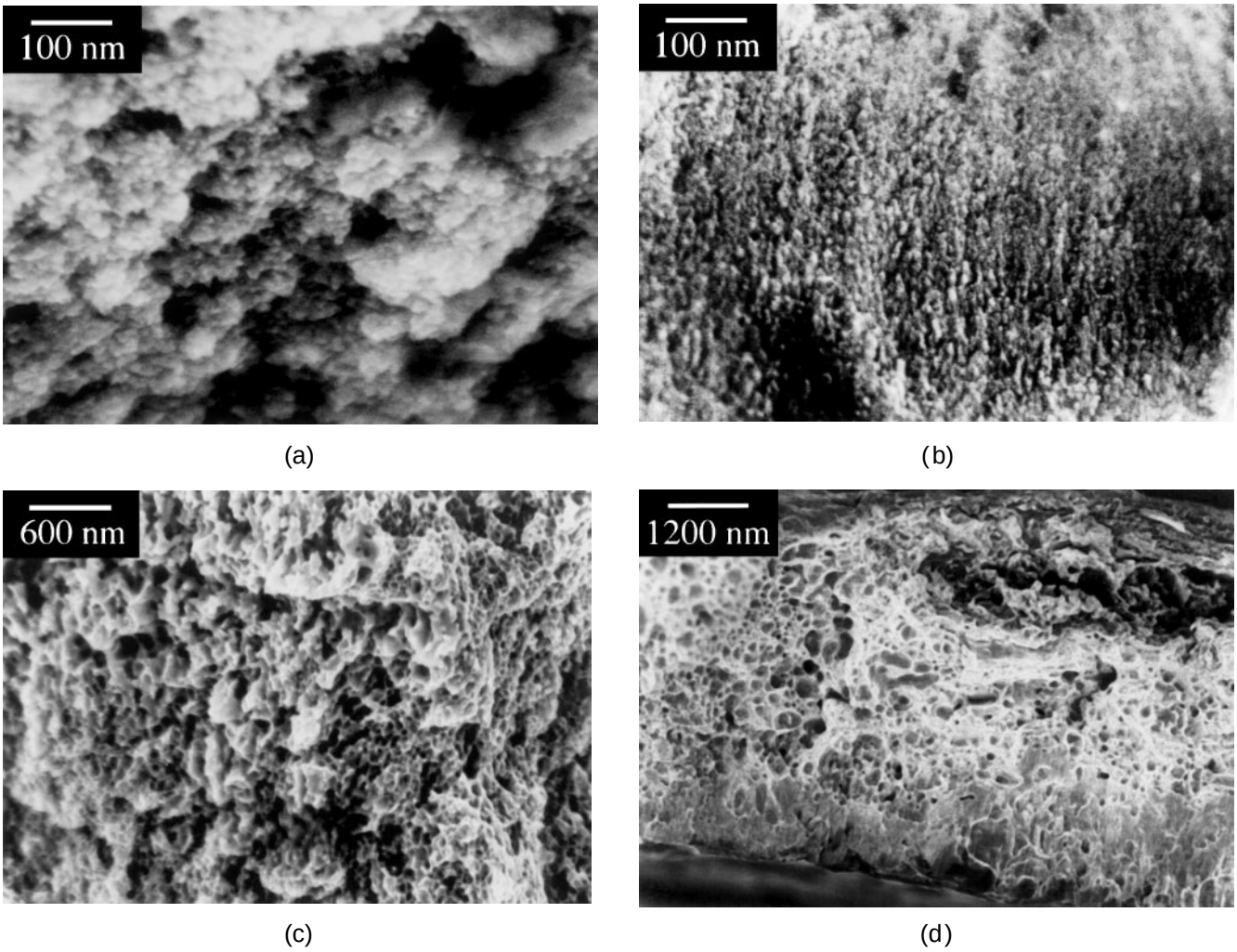

FIG. 4. SEM micrograph of room temperature-compacted *n*-Pd after fracture by bending (a). Samples were fractured after annealing for 100 min at 100 °C (b), 300 °C (c), or 800 °C (d).

became broader with increasing annealing temperature (Table IV). This broadening of the pore size distribution is especially evident when the volume-weighted pore distribution is plotted, as in Fig. 7. Note how the 300 °C anneal produced a significantly larger volume of pores in the 12 to 20 nm range. SANS from a *n*-Cu sample (2CuRT) was analyzed after it was annealed at 150 °C for 9 h in the SANS instrument [Fig. 6(b)]. As observed in the case of *n*-Pd, the average pore size increased, the number density decreased, and significant broadening of the size distribution occurred.

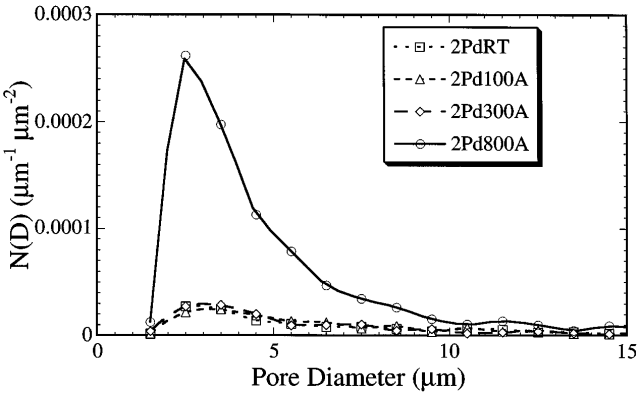

FIG. 5. Number-weighted (per unit area) pore distributions from image analysis of optical images of room temperature-compacted and annealed *n*-Pd.

C. Warm compaction

The hydrogen and oxygen impurity levels for warm compacted *n*-Pd and *n*-Cu are shown in Table III. Although the ratio of hydrogen to oxygen does not correspond to that of water, it is suspected that a primary

https://doi.org/10.1557/JMR.1996.0395 Published online by Cambridge University Press

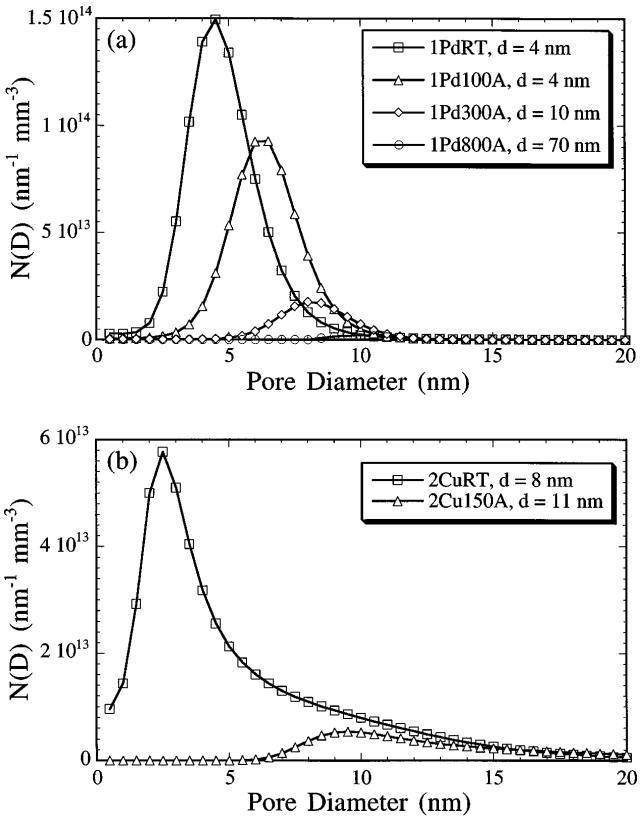

FIG. 6. Number-weighted pore distributions from the MaxSAS routine for room temperature-compacted and annealed *n*-Pd (a) and room temperature-compacted and annealed *n*-Cu (b).

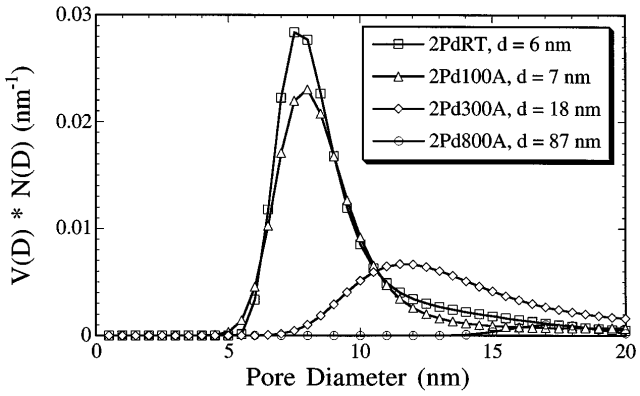

FIG. 7. Volume-weighted pore distributions from the MaxSAS routine for room temperature-compacted and annealed *n*-Pd.

source of the hydrogen contamination is water vapor condensed on the cold finger during powder collection. The cold finger acts as a cold trap, in addition to the one designed for that purpose. The hypothesis that the impurity gas is adsorbed on the clusters is supported by the observation that the hydrogen levels in both *n*-Pd and *n*-Cu were greatly reduced by warming the powder with a bakeout lamp prior to compaction (Table III, the starred samples). Further, the hydrogen level in *n*-Pd can be decreased by annealing (Table IV). Another source of hydrogen contamination may arise from the low pumping speed of hydrogen by turbomolecular pumps, which may lead to a significant concentration of residual hydrogen in the chamber prior to back-filling with helium (even though a titanium sublimation pump was used).

The effects of warm compaction on the pore size and distribution in *n*-Pd are shown in Figs. 8 and 9. A 100 °C compaction produced a somewhat smaller average pore size and approximately the same number density as did annealing at the same temperature (Fig. 8). However, a 300 °C compaction virtually eliminated the small pores (note the significant drop in scattering in Fig. 2). The volume-averaged pore distribution of Fig. 9 shows the dramatic impact of a 300 °C warm compaction on the pore population in the 5 to 20 nm regime. Although the

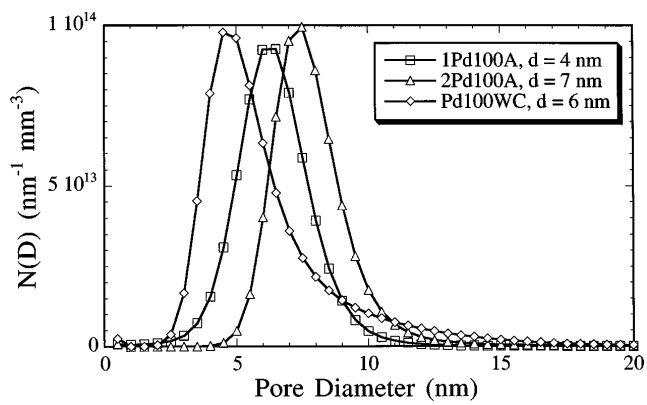

FIG. 8. Number-weighted pore distributions from the MaxSAS routine comparing the effects of annealing (two samples) and warm compaction at 100 °C for *n*-Pd.

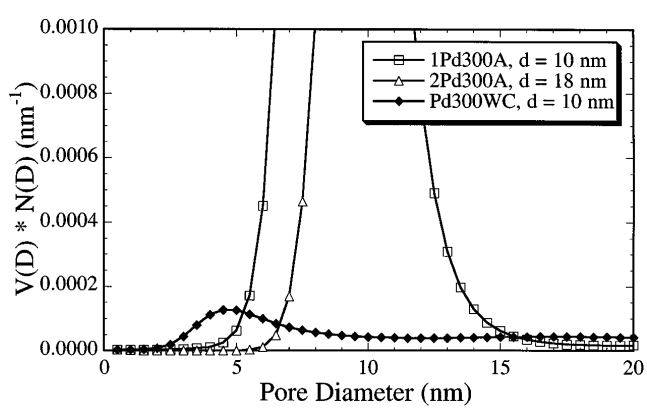

FIG. 9. Volume-weighted pore distributions from the MaxSAS routine comparing the effects of annealing (two samples) and warm compaction at 300 °C for *n*-Pd.

https://doi.org/10.1557/JMR.1996.0395 Published online by Cambridge University Press

300 °C warm compaction reduced the amount of porosity dramatically compared to annealing, the grain size was not increased significantly (Tables II and IV). There was some broadening of the pore distribution following the 300 °C compaction, but the number-averaged pore size was not any larger than that produced by annealing at the same temperature (Tables II and IV). The reduced number density of pores after warm compaction could result from lower hydrogen levels, which may decrease the formation of gas-filled pores.[32,34] Similar results were expected for *n*-Cu, but were not seen in the temperature range investigated.

SEM images taken of the as-compacted surfaces of *n*-Pd and *n*-Cu (Fig. 10) reveal some flaws, most likely resulting from imperfect particle rearrangement during compaction. The defects composed only 1–5% of the total surface area; thus the fields of view in Fig. 10 were not typical of the generally smooth and featureless surface. In Fig. 10(a), small, distinct, individual grains are seen in *n*-Pd compacted at 100 °C, as well as larger clusters of grains. Larger, more rounded, and sintered clusters are seen in *n*-Cu compacted at 150 °C [Fig. 10(b)], and it is more difficult to see the individual grains which comprise the clusters. This pronounced difference in appearance probably resulted from the higher homologous compaction temperature for the *n*-Cu ($0.3T_m$ compared to $0.2T_m$ for palladium).

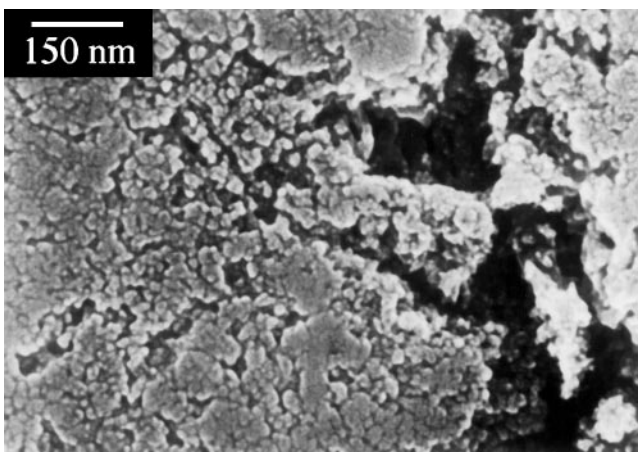

(a)

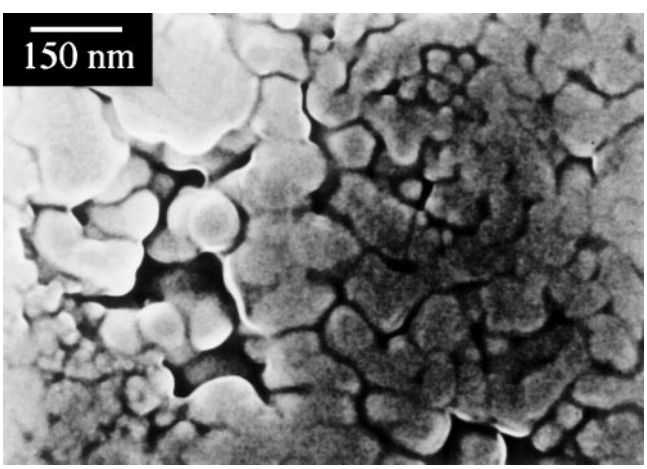

(b)

FIG. 10. SEM micrographs of the as-compacted surface of *n*-Pd compacted at 100 °C (a) and *n*-Cu compacted at 150 °C (b).

D. Hardness and fracture

Changes in hardness as a function of grain size, annealing, and warm compaction are shown in Fig. 11. The hardness of the room temperature-compacted *n*-Pd increased with decreasing grain size, indicating that strengthening was occurring with grain refinement.[35] Upon annealing at 100 °C, both 1PdRT and 2PdRT showed increased hardness,[36] perhaps due to better particle bonding (sintering or formation of lower energy boundaries).[37] The high compressive stresses in hardness testing may lead to deformation by generation and movement of dislocations.[38] Annealing and warm compaction may harden the material by eliminating boundary dislocation sources such as ledges. After this initial increase, the hardness decreased as the annealing temperature was raised, most likely as a result of grain growth. The increased hardness produced by annealing (as compared to room temperature-compacted samples having the same grain size) was maintained throughout the grain size range of the data. The data point for the sample compacted at 100 °C, which had a density and hydrogen level similar to 1PdRT, fit on the annealing curve for 1PdRT.

The sample compacted at 300 °C had a hardness of 5.8 GPa, almost double that of other samples at this

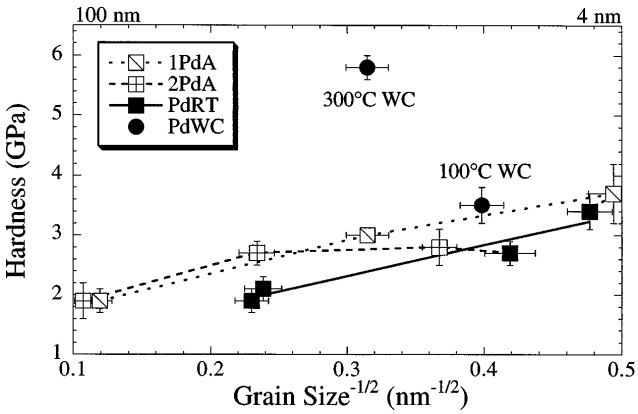

FIG. 11. Vickers microhardness vs the square root of the reciprocal grain size for room temperature-compacted, annealed, and warm compacted *n*-Pd. The solid line is a least squares fit to the room temperature-compacted samples (filled squares). Dashed lines depict changes in hardness of sample quarters annealed at progressively higher temperatures.

https://doi.org/10.1557/JMR.1996.0395 Published online by Cambridge University Press

grain size. This substantial increase in hardness was also observed in five samples of *n*-Pd compacted at 200 °C. These samples, which had grain sizes, hydrogen contents, and densities similar to Pd300WC, all had hardnesses greater than 5 GPa. This increased strength may result from the higher sample density, which could be driven by the combination of lower hydrogen contamination and better sintering of the grains. While warm compaction drives off the vast majority of gaseous impurities, it may also make it kinetically more favorable for the remaining contaminants to form compounds with the metal, which would also harden the material.

Sample quarters receiving the same treatment as 1PdRT were broken by bending, with the bending stress applied about a horizontal axis with respect to the SEM pictures (Fig. 4). Surface details due to grains were seen in the room temperature-compacted and 100 °C annealed samples [Figs. 4(a) and 4(b)]. The fracture mode appeared to be intergranular, with the grains in Fig. 4(b) appearing somewhat elongated along the fracture direction (most of the fracture surface was not flat enough to see this effect). As seen in Fig. 10(a), the grains in Fig. 4(a) seem to be grouped into clusters. This hierarchical structure may have an impact on the deformation behavior. In the case of the samples annealed at 300 and 800 °C, the fracture surface appeared much more ductile [Figs. 4(c) and 4(d)]. The significant number of large pores, especially in the 800 °C sample, could have made the fracture surface appear ductile even though there was very limited deformation.

V. SUMMARY

Analysis of the SANS data from room temperature-compacted *n*-Pd and *n*-Cu indicated a high concentration of hydrogen impurities, as well as pore sizes and number densities which scaled with grain size. Annealing decreased the hydrogen level and number of pores, but at the same time increased the grain and pore sizes. Warm compaction of *n*-Pd also decreased the hydrogen concentration and dramatically reduced the number density of pores, while only slightly increasing the grain size. These effects led to higher densities for *n*-Pd. Hardness and fracture characteristics appeared to be directly related to the compaction and annealing conditions.

These findings show that progress has been made toward producing nanocrystalline materials in which the properties are not dominated by extrinsic effects. However, as the minimal response of *n*-Cu to warm compaction illustrates, further improvements are necessary. Recently, a new synthesis chamber was designed and built.[13] Some of the improved capabilities include a base vacuum an order of magnitude better than the old chamber (from $\approx 4 \times 10^{-5}$ to 4×10^{-6} Pa), the ability to evaporate in a flowing atmosphere (changing gas every 10 min), and a larger collection surface. Typical *n*-Cu samples have gone from 0.1 to 0.2 mm thick to 0.2 to 0.5 mm, and from 90–95% to 95–99% dense. These improvements are a direct result of the cleaner powders and larger quantities of material produced. Preliminary indications are that the new synthesis chamber, with its cleaner environment, has improved the average density and impurity level in *n*-Cu to better than that achieved in this study by warm compaction of *n*-Pd. Further SANS measurements are needed to confirm these observations.

ACKNOWLEDGMENTS

This work was supported by the U.S. Department of Energy, Office of Basic Energy Science-Materials Science, under Grant DE-FG02-86ER45229 at Northwestern University and Contract W-31-109-Eng-38 at Argonne National Laboratory, and by the National Science Foundation, Agreement DMR-9122444, at the National Institute of Standards and Technology. One author (P. G. S.) acknowledges a fellowship from the Office of Naval Research. Special thanks to P. R. Jemian for supplying the MaxSAS code, documentation, and valuable suggestions. Thank you also to A. J. Allen for informative discussions on the globular form factor.

REFERENCES

1. H. Gleiter, Prog. Mater. Sci. **33**, 223 (1989).
2. X. Zhu, R. Birringer, U. Herr, and H. Gleiter, Phys. Rev. B **35**, 9085 (1987).
3. T. Haubold, R. Birringer, B. Lengeler, and H. Gleiter, Phys. Lett. A **135**, 461 (1989).
4. J. A. Eastman, M. R. Fitzsimmons, and L. J. Thompson, Philos. Mag. B **66**, 667 (1992).
5. G. J. Thomas, R. W. Siegel, and J. A. Eastman, Scripta Metall. Mater. **24**, 201 (1990).
6. E. A. Stern, R. W. Siegel, M. Newville, P. G. Sanders, and D. Haskel, Phys. Rev. Lett. **75**, 3874 (1995).
7. E. Jorra, H. Franz, J. Peisl, G. Wallner, W. Petry, R. Birringer, H. Gleiter, and T. Haubold, Philos. Mag. B **60**, 159 (1989).
8. J. E. Epperson, R. W. Siegel, J. W. White, J. A. Eastman, Y. X. Liao and A. Narayanasamy, in *Neutron Scattering for Materials Science*, edited by S. M. Shapiro, S. C. Moss, and J. D. Jorgenson (Mater. Res. Soc. Symp. Proc. **166**, Pittsburgh, PA, 1990), p. 87.
9. P. G. Sanders, J. R. Weertman, J. G. Barker, and R. W. Siegel, in *Molecularly Designed Ultrafine/Nanostructural Materials*, edited by K. E. Gonsalves, G-M. Chow, T. D. Xiao, and R. C. Cammarata (Mater. Res. Soc. Symp. Proc. **351**, Pittsburgh, PA, 1994), p. 319.
10. P. G. Sanders, J. R. Weertman, J. G. Barker, and R. W. Siegel, Scripta Metall. Mater. **29**, 91 (1993).
11. H-E. Schaefer, in *Mechanical Properties and Deformation Behavior of Materials Having Ultra-Fine Microstructures*, edited by M. Nastasi, D. M. Parkin, and H. Gleiter (Kluwer, Dordrecht, 1993), p. 81.
12. R. Würschum, M. Scheytt, and H-E. Schaefer, Phys. Status Solidi (a) **102**, 119 (1987).
13. A. J. Allen, S. Krueger, G. G. Long, H. M. Kerch, H. Hahn, and G. Skandan, Nanostruct. Mater. **7**, 113 (1995).
14. P. G. Sanders, G. E. Fougere, L. J. Thompson, J. A. Eastman, and J. R. Weertman, unpublished.

https://doi.org/10.1557/JMR.1996.0395 Published online by Cambridge University Press

15. R. W. Siegel, S. Ramasamy, H. Hahn, Z. Li, T. Lu, and R. Gronsky, J. Mater. Res. **3**, 1367 (1988).
16. K. Kimoto, J. Phys. Soc. Jpn. **8**, 762 (1953).
17. H. Gleiter, in *Deformation of Polycrystals: Mechanisms and Microstructures*, edited by N. Hansen, A. Horsewell, T. Leffers, and H. Lilholt (Risø National Laboratory, Roskilde, 1981), p. 15.
18. B. E. Warren, *X-ray Diffraction* (Dover, New York, 1990), p. 251.
19. P. G. Sanders, A. B. Witney, J. R. Weertman, R. Z. Valiev, and R. W. Siegel, Mater. Sci. Eng. A **204**, 7 (1995).
20. R. T. Ratcliffe, Brit. J. Appl. Phys. **16**, 1193 (1965).
21. R. M. Lindstrom, J. Res. NIST **98**, 127 (1993).
22. W. D. Ehmann and B-F. Ni, J. Radioanal. Nuc. Chem. **160**, 169 (1992).
23. B. Hammouda, S. Krueger, and C. J. Glinka, J. Res. NIST **98**, 31 (1993).
24. G. Porod, in *Small Angle X-ray Scattering*, edited by O. Glatter and O. Kratky (Academic, London, 1982), p. 17.
25. A. Guinier and F. Fournet, *Small Angle Scattering of X-rays* (Wiley, New York, 1955).
26. J. A. Potton, G. J. Daniell, and B. D. Rainford, J. Appl. Crystallogr. **21**, 891 (1988).
27. P. R. Jemian, personal communication.
28. A. J. Allen, J. Appl. Crystallogr. **24**, 624 (1991).
29. P. R. Jemian and A. J. Allen, J. Appl. Crystallogr. **27**, 693 (1994).
30. T. Kizuka, Y. Nakagami, T. Ohata, I. Kanazawa, H. Ichinose, H. Murakami, and Y. Ishida, Philos. Mag. A **69**, 551 (1994).
31. A. Tschöpe and R. Birringer, Philos. Mag. B **68**, 223 (1993).
32. J. S. Reed, *Introduction to the Principles of Ceramic Processing* (Wiley, New York, 1988), p. 449.
33. T. H. Courtney, *Mechanical Behavior of Materials* (McGraw-Hill, New York, 1990), p. 649.
34. X. Y. Qin, X J. Wu, and L. D. Zhang, Nanostruct. Mater. **5**, 101 (1995).
35. G. W. Nieman, J. R. Weertman, and R. W. Siegel, Scripta Metall. **23**, 2013 (1989).
36. A. H. Chokshi, A. Rosen, J. Karch, and H. Gleiter, Scripta Metall. **23**, 1679 (1989).
37. G. E. Fougere, J. R. Weertman, R. W. Siegel, and S. Kim, Scripta Metall. Mater. **26**, 1879 (1992).
38. W. B. Li, J. L. Henshall, R. M. Hooper, and K. E. Easterling, Acta Metall. **39**, 3099 (1991).

https://doi.org/10.1557/JMR.1996.0395 Published online by Cambridge University Press